Available online at www.CivileJournal.org

Civil Engineering Journal

(E-ISSN: 2476-3055; ISSN: 2676-6957)

Vol. 12, No. 02, February, 2026

Structural Performance of Circular Hollow Steel Damper with Fins and Gaps

Tobok S. M. Aritonang [1, 2], Iman Satyarno [1], Ali Awaludin [1*], Angga F. Setiawan [1]

[1] Department of Civil and Environmental Engineering, Universitas Gadjah Mada, Sleman, Indonesia.

[2] Department of Civil Engineering, Universitas Cenderawasih, Jayapura, Indonesia.

Received 05 March 2025; Revised 18 December 2025; Accepted 22 December 2025; Published 01 February 2026

Abstract

Prior studies have shown that fin reinforcement on a circular hollow steel damper (CHSD) could mitigate buckling and enhance shear strength. However, in bridge applications, repeated vibrations from lateral traffic loads and low-frequency cyclic actions may cause premature energy dissipation and fatigue damage, thus reducing the seismic performance of CHSD during design-level earthquakes. To address this issue, this study integrates fins and gaps into CHSD to enhance stability against buckling and to mitigate fatigue-induced damage. The CHSD specimens were fabricated in three variations: without fins, with fins, and with fins and gaps. Cyclic loading tests and nonlinear finite element analyses were conducted to evaluate their effects on mechanical properties and seismic performance. Cyclic loading was performed in accordance with the AISC 341-22 protocol and applied at 0° and 30° to simulate multidirectional lateral forces. The cyclic test results reveal that the addition of fins exhibits both beneficial and adverse effects on the mechanical properties and seismic performance of CHSD, while the gap reduces the equivalent viscous damping ratio. The backbone curves derived from the numerical analyses agree well with experimental results. Furthermore, the damper shear resistance and deformation capacity are delayed by the presence of gaps, mitigating fatigue-related damage.

Keywords: Circular Hollow Steel Damper (CHSD); Fins; Gaps; Cyclic Loading; Equivalent Viscous Damping Ratio.

1. Introduction

Structural control systems have been extensively investigated to find novel means towards preventing or reducing damage to bridge structures caused by dynamic loads. These systems are generally classified into four categories: passive, semi-active, active, and hybrid control systems [1, 2]. Among them, passive control systems are the most widely adopted because they provide additional damping and stiffness without requiring an external energy source [3]. Passive systems dissipate seismic energy through inelastic deformation or friction, while the primary gravity load-bearing structural components can be designed to remain elastic [4]. Structures without dampers instead directly absorbed seismic energy through their structural components, resulting in large deformations and enhancing damage potential. Various types of passive dampers have been developed and implemented, including viscoelastic, metallic, friction, tuned mass, and tuned liquid dampers [5-7]. Metallic dampers have the most effective absorption of seismic energy in the structure, with energy dissipation occurring through the inelastic deformation of metal materials [7].

Metallic dampers are classified according to their constitutive materials, namely steel dampers, aluminium dampers, lead dampers, copper dampers, and shape memory alloy dampers [3]. A widely employed steel damper in seismic design is the shear panel damper (SPD) [8-10], which consists of web and connection plates welded together, as illustrated in Figure 1-a. The web plate is the primary component resisting lateral loads, while the connection plates attach the SPD to the structure. Typically, web plates are fabricated from low-yield-point (LYP) steels with high ductility and elongation

* Corresponding author: ali.awaludin@ugm.ac.id

https://doi.org/10.28991/CEJ-2026-012-02-03

capacity, ensuring that their yield strength is significantly lower than that of the main structure while maintaining greater deformation. LYP steels such as LY100, LY160, and LY225 are recommended as damper materials due to their favorable combination of low yield strength, high ductility, and effective energy dissipation capacity [11, 12]. However, the deformation capacity of SPDs is often reduced due to local buckling failure of the web plate. One method to mitigate this local buckling issue is the addition of stiffening plates to the web plate, as shown in Figure 1-b.

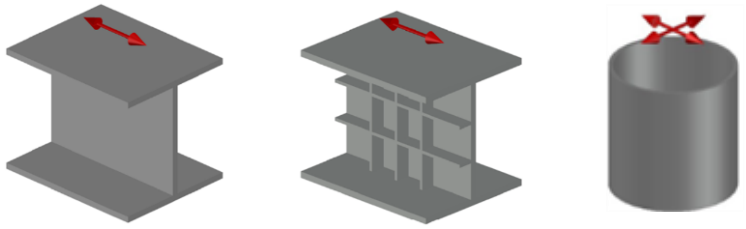

(a) (b) (c)

Figure 1. Illustration of: a) SPD without stiffeners, b) SPD with stiffeners, and c) vertical pipe damper (VPD) [3]

Extensive studies have investigated the local buckling problems, mechanical behavior, and seismic performance of SPDs. Zhang et al. [13] verify the mechanical properties of SPD and the fatigue characteristics under low cycles. An analysis was also conducted on the hysteretic behavior of low-grade steel SPD under various loading conditions [14]. Zhang et al. [15] explore the relationship between the buckling ratio and the deformation capacity of SPD. Tanaka & Sasaki [9] verify the hysteretic performance by varying the width-to-thickness ratio (d/t_w), and the results showed that the SPD performance was excellent when the ratio was less than 40. Subsequently, Chen et al. [16], Ge et al. [17], and Lin et al. [18] investigated the effect of stiffeners and observed their significant effectiveness in preventing local buckling failure of the web plate. Pan et al. [19] demonstrate that the energy dissipation capacity of low-yield-point steel shear panel damper (LSSPD) increases with shear plate area, and stiffeners enhance ultimate strength. Their relative placement may, however, reduce this capacity. Shang et al. [20] investigate the mechanical behavior of SPD with and without stiffeners under unidirectional and bidirectional loading. Their results reveal differences in failure modes, yielding behavior, and stress distribution of the SPDs under bidirectional loading. Furthermore, the in-plane yield force of SPD decreases as the loading direction increases, which may lead to an overestimation of its bidirectional performance in structural design.

Several studies on the application of SPDs as a damping device in bridge structures have demonstrated their great potential to reduce seismic demands and enhance seismic performance. Aoki et al. [21] develop a new SPD that acts as a lateral shear load resistor, installed on continuous girder bridges. The results showed that SPD could significantly reduce expansion joint displacements and the forces acting on the columns by approximately 25%. Fajar et al. [22] conduct a study on the pile-supported slab viaduct (PSSV) structure, reinforced with steel bracing and additional SPD. The results show that the PSSV structure with SPD exhibits significantly higher seismic performance than the regular structure. Ge et al. [23] also examine the effect of installing SPD as a structural control device on a bridge pier structure. However, due to its flat-plate configuration, SPD is limited to dissipating energy in only one loading direction – a constraint, given seismic forces are inherently multidirectional. This highlights the need to develop SPD shapes and configurations capable of resisting lateral shear loads from multiple directions.

Numerous studies have developed different shear damper configurations and evaluated their ability to resist lateral shear loads from multiple directions. One such damper is the vertical pipe damper (VPD) (see Figure 1-c) [3], also referred to as the circular hollow steel damper (CHSD) [24], which is fabricated from a vertical steel pipe welded to the top and bottom baseplates. Abebe et al. [24] verify that CHSD can withstand multidirectional loads. Under cyclic loading, the initial circular shape deforms into an elliptical shape, enabling additional energy absorption. The failure mode of the CHSD depends on the height-to-diameter ratio (H/D), where $H/D > \sqrt{3}$ indicates flexural failure, while $H/D < \sqrt{3}$ corresponds to shear failure. To prevent local buckling failure and enhance the structural performance of the CHSD, several researchers have proposed installing vertical fin plates on the tube wall [25-27]. These fins delay local buckling, improve shear strength and lateral stiffness, and increase both energy dissipation capacity and hysteretic damping. To address premature failure at the tube ends, the use of inner short pipes has also been proposed as a reinforcement strategy [28]. Other developments in shear damper design include the hollow-box [29, 30] and crossing-web configurations [31].

In bridge applications, repeat vibrations from lateral traffic loads and low-frequency cyclic actions facilitate premature energy dissipation and long-term fatigue damage. Several researchers have proposed incorporating a gap mechanism in dampers to address fatigue issues [32-35]. A gap mechanism allows the damper to remain inactive under small cyclic loads, preventing unnecessary degradation. The damper engages only when the displacement exceeds the gap length, allowing significant energy dissipation during seismic events, extending service life, and ensuring optimal seismic performance. Several studies have investigated the application of shear panel dampers with a gap (SPDG) in bridges. Setiawan [32] developed an SPDG device applied to a bridge pier integrated with a steel pipe column, where the gaps were intended to prevent deterioration of damper performance caused by daily loading and cyclic fatigue from frequent lateral deformations. Emilidardi et al. [33] apply SPDG to a pre-stressed concrete girder (PCI girder) bridge.

The seismic performance of the bridge was then analyzed using nonlinear time-history analysis, with the results showing that installing SPDG on the bridge structure improved seismic performance. Haroki et al. [34] compared the seismic performance of simply supported hollow slab on pile group (SHSPG) structures designed as "critical" and "essential" viaducts using SPDG devices. Santoso et al. [35] proposed the use of SPDG as a replacement for lead rubber bearing (LRB) in simply supported prestressed concrete (PSC) box girder bridges. The replacement was considered because LRB has high costs, while SPDG offers a more cost-effective solution and provides high damping capacity. These findings suggest that SPDG can be applied in seismic isolation systems due to similar performance with LRB. However, to date, no experimental or numerical studies have examined the structural performance of CHSD combining fin reinforcement and gap installation. Previous research has investigated CHSD with fins or SPDs with a gap mechanism separately, but studies integrating both approaches remain limited.

This study develops a new type of CHSD incorporating fin reinforcement and gaps. The advancement of CHSD with fins and gaps can have significant practical implications for bridges in high seismic zones, particularly those with simple support systems employing piers with roller or rubber bearings. In this configuration, the CHSD is expected to dissipate seismic energy through relative deformation between the superstructure and bearings, reducing cyclic damage and extending the bridge's service life. The CHSD consists of a hollow circular component, fins, and a base plate, which were welded together. The circular hollow steel tube serves as the main component for dissipating seismic energy. A circular shape is preferred over hollow-box or cross-web typologies, given the uniformity of shear strength in all loading directions. This is preferable for seismic loads, since they act in a multidirectional manner [24]. Experimental testing and numerical analyses using the finite element method were conducted to evaluate the structural performance of the proposed CHSD. The evaluations included hysteresis curves, shear strength, initial stiffness, energy dissipation, equivalent viscous damping ratio, deformation, and failure modes. However, this study has a limitation in that fatigue testing of the CHSD specimens could not be conducted due to laboratory constraints. Therefore, future research is expected to address this limitation to evaluate the long-term fatigue performance of the proposed CHSD.

2. Experimental Preparation

In this study, the steel used for energy dissipation was required to have a low yield point, with a target yield strength below 225 MPa [11]. The CHSD specimen design considered the capacity of the laboratory testing facilities, and the 3-D finite element model was analyzed using Abaqus software. Figure 2, shows the flowchart of the research methodology through which the objectives of this study were achieved.

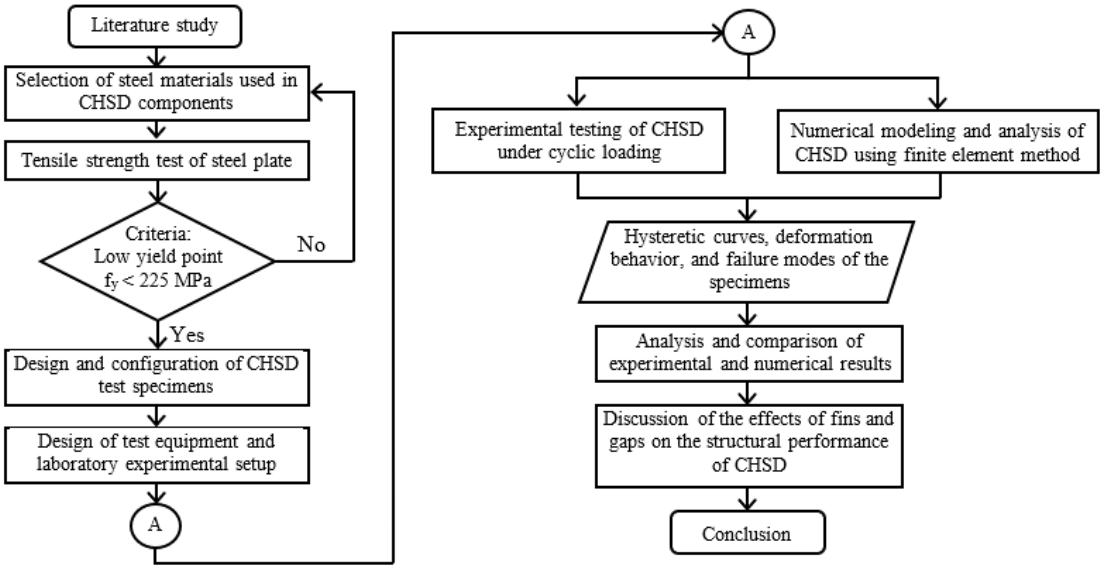

Figure 2. Flow chart of the research

2.1. Test Specimen Configuration

Two types of CHSD specimens at a 1:2 scale were tested in this study, namely CHSD without fins (CHSD-NF) and with fins (CHSD-F), as shown in Figure 3. The CHSD-NF specimen consists of the circular hollow steel component and a baseplate, while the CHSD-F specimen includes the same components with the addition of fin plates. The circular hollow steel has an outer diameter of 120 mm, a height of 100 mm, and a thickness of 2.8 mm, with baseplate and fin plate thicknesses of 12 mm and 4.8 mm, respectively. Since the height-to-diameter ratio of 0.83 is less than $\sqrt{3}$, the failure mode is shear [24]. The circular hollow steel is connected to the baseplate with a 5 mm thick angle weld using SMAW E-7018 electrodes. For the CHSD-F specimen, six fin plates are vertically mounted on the tube and welded along their edges. In this study, the welding quality of the CHSD specimens was not analyzed and is assumed to meet theoretical expectations. However, the quality and completeness of the welding process are crucial to ensure specimen homogeneity. In future applications, CHSD fabrication will be directed toward moulding methods once the prototype demonstrates adequate performance.

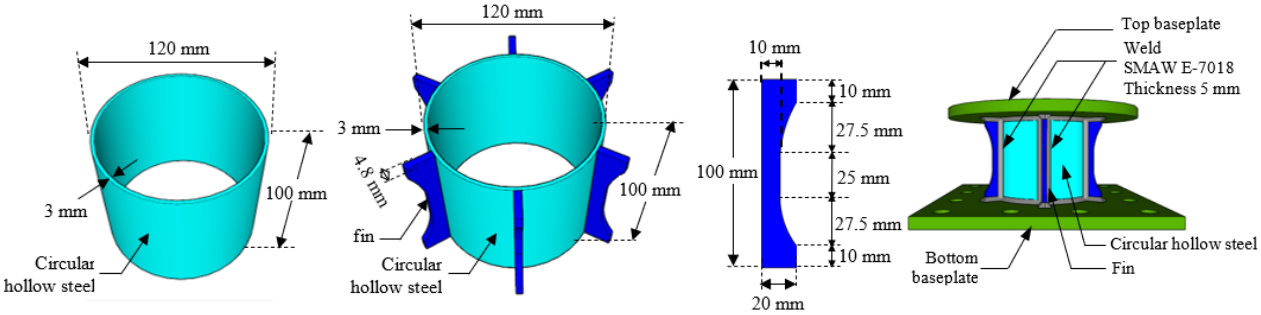

(a) (b) (c) (d)

Figure 3. Components of the CHSD specimen: (a) circular hollow component without fins, (b) circular hollow component with fins, (c) fins detail, and (d) weld connection between the tube, fins, and baseplate

The configuration of the CHSD test specimens is shown in Table 1 and Figure 4. CHSD with fins (CHSD-F) was further divided into specimens without a gap (CHSD-F) and with a gap (CHSD-F-G). For the TSPD-F-G specimens (see Figure 4-c), gaps were placed on the side and top of the top base plate, with a length of 5 mm and 1 mm, respectively. The gap length is determined based on the maximum lateral displacement of the bridge slab due to lateral service loads, which requires 5 mm. A gap on the top side of the plate is provided to prevent axial forces on the SPD. To simulate lateral loads from multiple directions, cyclic loading was applied at two angles: 0° and 30°. These loading directions were set according to the angle formed by the fin plate relative to the x-axis, as shown in Figure 5. The CHSD offers a simple fabrication process, as the circular hollow steel component can be formed from a steel plate welded into a tube, with optional fins attached and welded in place. Its ability to resist multidirectional lateral loads allows a single unit to be used in bridge structures, offering cost efficiency. In contrast, SPDs work in only one direction, requiring two units for multidirectional resistance, which increases fabrication costs.

Table 1. The configuration of the CHSD specimen

No	Test Specimen	H (mm)	D (mm)	t (mm)	t_f (mm)	H/D	*Fin*	*Gap*	Loading direction (°)
1	CHSD-NF	100	120	2.8	-	0.83	-	-	-
2	CHSD-F-0	100	120	2.8	4.8	0.83	√	-	0
3	CHSD-F-30	100	120	2.8	4.8	0.83	√	-	30
4	CHSD-F-G-0	100	120	2.8	4.8	0.83	√	√	0
5	CHSD-F-G-30	100	120	2.8	4.8	0.83	√	√	30

Note: H = specimen height; D = specimen diameter; t = circular hollow thickness; t_f = fin thickness

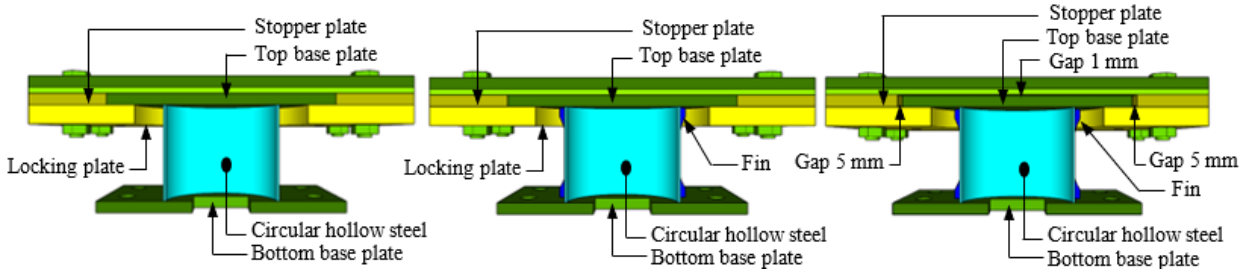

(a) CHSD-NF (b) CHSD-F (c) CHSD-F-G

Figure 4. CHSD specimen configuration

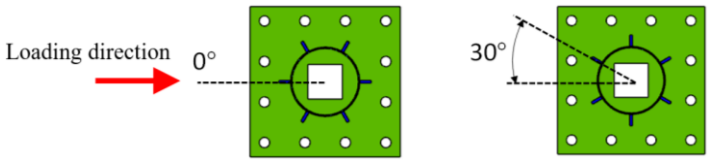

(a) 0° (b) 30°

Figure 5. Variation of loading direction

2.2. Material of CHSD Test Specimen

In the CHSD test specimen configuration (Figure 4), the circular hollow component is made from a cold-rolled steel plate (SPCC) material conforming to the Japanese standard JIS-G3141. SPCC steel was selected to ensure a lower yield

strength suitable for energy dissipation. Because SPCC plates are available in limited thicknesses and fin plates require thicker material than the web plate (i.e., the circular hollow steel wall of the CHSD), hot-rolled steel plates (SPHC) were used for the fins to achieve the required thickness. SPHC conforms to the Japanese standard JIS-G3131. The material used for the base plate component and the plates added to the top base plate was mild steel SS400. To determine the mechanical properties, the SPCC and SPHC materials were subjected to a tensile test using a universal testing machine (UTM) in accordance with the Indonesian national standard for metal tensile tests [36]. The dimensions of the test specimens and the tensile testing process are shown in Figure 6. SS400 was not subjected to tensile testing, as it is used for the base and additional plates, which are designed to remain elastic.

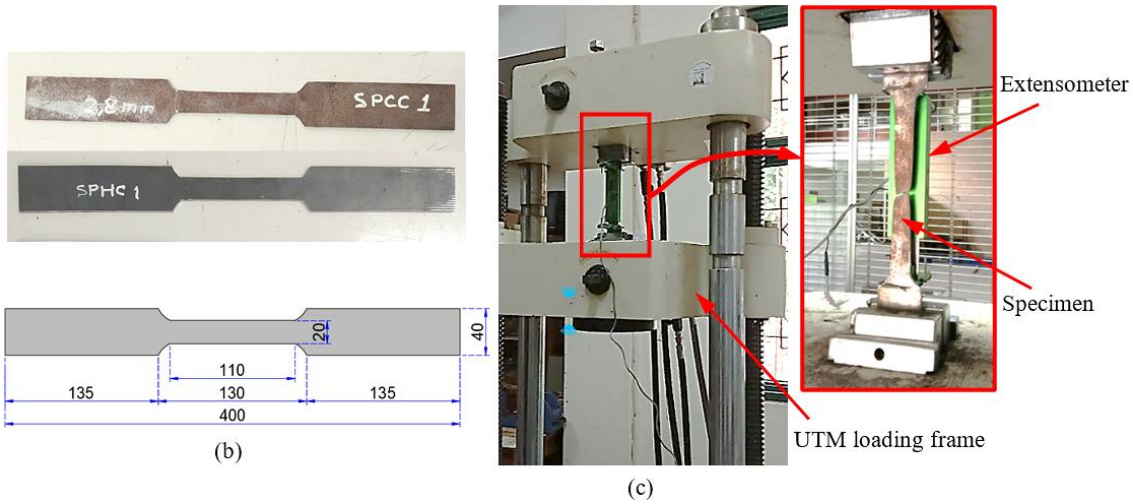

Figure 6. (a) SPHC and SPCC tensile specimens, (b) dimensions of the specimen (mm), and (c) tensile test process

2.3. Experimental Setup and Cyclic Loading Protocol

Cyclic testing of all CHSD specimens was conducted using a loading frame and hydraulic jack, as shown in Figure 7. Both devices were installed on a rigid floor using anchors to ensure that the testing equipment was securely attached and stable, preventing any reading errors caused by deformation of the loading frame. A load cell with a capacity of 500 kN was installed between the hydraulic jack and the loading beam to measure the magnitude of shear force transmitted through the hydraulic jack. The top base plate of the specimen was attached to the loading beam using bolts. The loading beam was able to move horizontally to accommodate the cyclic shear load. Furthermore, the bottom base plate of the specimen was fitted on supports and clamped in all directions. Shear force was transmitted from the hydraulic jack to the loading beam and the CHSD specimen, causing displacement to occur only at the top base plate. The displacement of the CHSD specimen and the loading frame was measured using LVDT 1 and LVDT 2, respectively. Cyclic loading was applied gradually until the target displacement was reached as planned. Figure 8 shows a photograph of the specimen and test setup. In this experiment, cyclic loading was applied with displacement control according to AISC 341-22 [37]. For CHSD-F-G, a gap length of 5 mm was added to the target displacement, and Figure 9 presents the cyclic loading history.

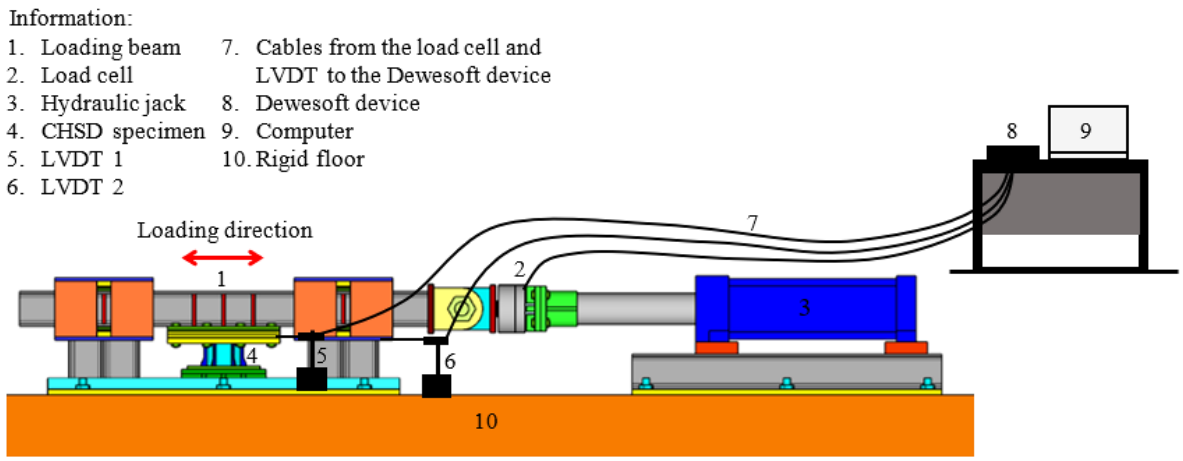

Figure 7. Schematic of the CHSD test setup

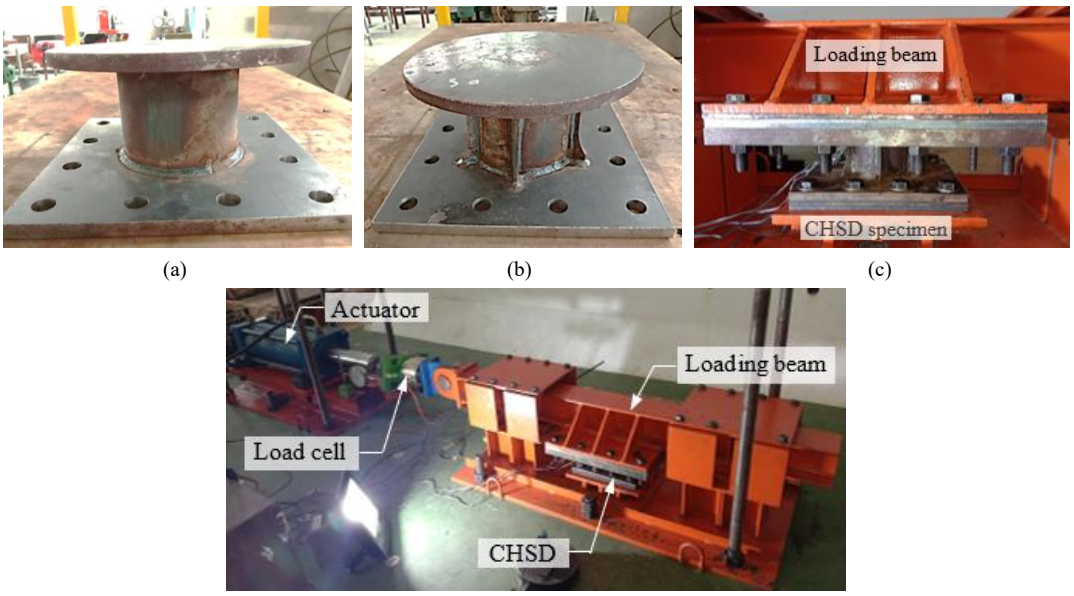

(a) (b) (c)

(d)

Figure 8. (a) CHSD without fins, (b) CHSD with fins, (c) specimen placement on the loading frame, and (d) test setup

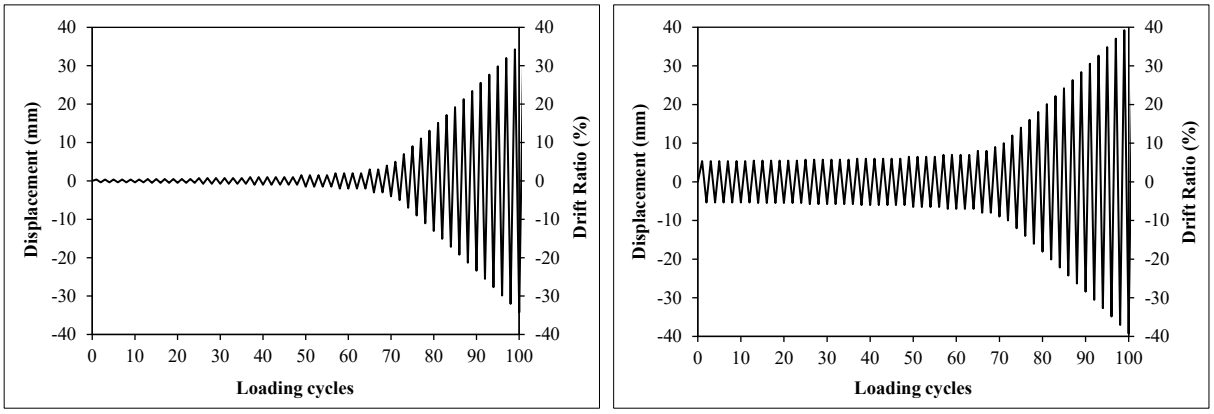

(a) (b)

Figure 9. Cyclic loading history: (a) without gaps, and (b) with gaps

2.4. Mechanical Behavior and Seismic Performance Evaluation Method of CHSD

The shear strength of CHSD with a fin was obtained by integrating the shear stresses in the web and fin components [27]. According to AISC 360-16 [38], the web shear yield strength (V_{yw}) was determined using Equation 1, where f_y is the tensile yield stress of steel and A_g is the member's gross cross-sectional area. The factor 0.6 represents the relationship between the shear yield stress (τ_y) and the tensile yield stress (f_y), indicating that the shear yield stress is approximately 60% of the tensile yield stress.

$$V_{yw} = \frac{0.6 f_y A_g}{2} \quad (1)$$

Furthermore, Awaludin et al. [27] proposed a formula to determine the shear strength contributed by the fin components of the CHSD (V_{yf}), as expressed in Equation 2, where A_{fi} denoted the cross-sectional area of the fin, τ_{f0} was the shear stress of the fin at 0°, β was the angle coefficient calculated using Equation 3, and θ represents the angle formed by each fin relative to the shear loading direction.

$$V_{yf} = \frac{\tau_y A_{fi} \beta}{2} \quad (2)$$

$$\beta = \left(1 - \frac{\tau_{f0}}{\tau_y}\right) sin(\theta) + \frac{\tau_{f0}}{\tau_y} \quad (3)$$

The shear strength of the CHSD was obtained by summing the shear strength contributions of the web and fin components, as expressed in Equation 4, where A_w denoted the cross-sectional area of the web, and k denoted the web coefficient. The proposed Equation 4 can be used to determine the shear yield strength of finned CHSDs, both slender and stocky [27].

$$V_y = \tau_y A_w k + \sum_{i=0}^{n} \frac{\tau_y A_{fi} \beta}{2} \quad (4)$$

The yield strength and yield displacement were also determined from the backbone curve obtained from the cyclic test results using the equivalent elastoplastic yield method (Figure 10) [39]. Meanwhile, the yield strength was determined by drawing a straight line connecting the yield displacement point on the backbone curve to the ordinate axis. The intersection point with the ordinate axis represents the yield strength of the CHSD. The ultimate displacement and strength corresponded to the conditions when the backbone curve reached the maximum force or just before a decrease in strength occurred. Subsequently, the stiffness of the CHSD was obtained by dividing the yield strength by its displacement.

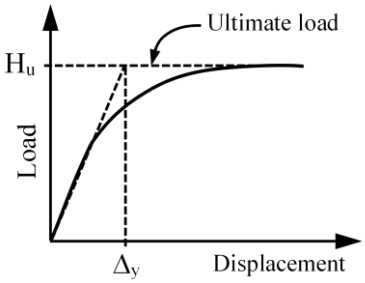

Figure 10. Definition for yield displacement [39]

The cumulative hysteretic energy dissipated was also calculated by adding the areas covered by the hysteresis curve in a specific loading cycle. The cumulative hysteretic energy was calculated according to JGJ 101-201 [26] using Equation 5, where E_p was the cumulative hysteretic energy, $Q_{(i)}$ was the force in each loading cycle, and $\Delta_{(i)}$ denoted the displacement in each cycle.

$$E_p = \sum_{i=1}^{n} \frac{(Q_{(i+1)}+Q_{(i)})}{2} \times (\Delta_{(i+1)} - \Delta_{(i)}) \quad (5)$$

The equivalent viscous damping ratio (ξ_{hys}) was a common index used to evaluate a damper's ability to dissipate energy. This ratio was calculated using Equation 6 [40], where E_{hys} was the damping hysteretic energy per cycle, equal to the area enclosed by the hysteresis curve, and E_{el} was the elastic displacement energy corresponding to the ultimate displacement in one complete loading cycle.

$$\xi_{hys} = \frac{E_{hys}}{4\pi E_{el}} \quad (6)$$

3. Result and Discussion

3.1. Mechanical Properties of Steel Materials

According to the test result in Figure 11 and Table 2, the shear yield stress of SPCC steel was less than 225 MPa (see Figure 2), rendering it a low-yield-point steel and therefore suitable for use as an energy dissipation component in CHSD. The yield strength of SPCC steel was also lower compared to SPHC. This result provides an opportunity for the circular hollow component made of SPCC steel to yield earlier than fin components and absorb energy more rapidly. The ultimate stress-to-yield stress ratio (f_u/f_y) for SPCC and SPHC steel is 1.40 and 1.24, respectively. The elongation value in Table 2 is the ratio of the specimen's length at rupture to its original length, expressed as a percentage (%). Based on the results, the elongation of SPCC steel is 1.67 times greater than that of SPHC, indicating greater ductility. The mechanical properties of SPCC steel were similar to those of BLY160 steel used by Zhu et al. [4] for the construction of SPD, where the study reported f_y= 203 MPa, f_u = 304 MPa, and the ratio of f_u/f_y = 1.49. These material properties of BLY160 steel meet seismic design standards in China.

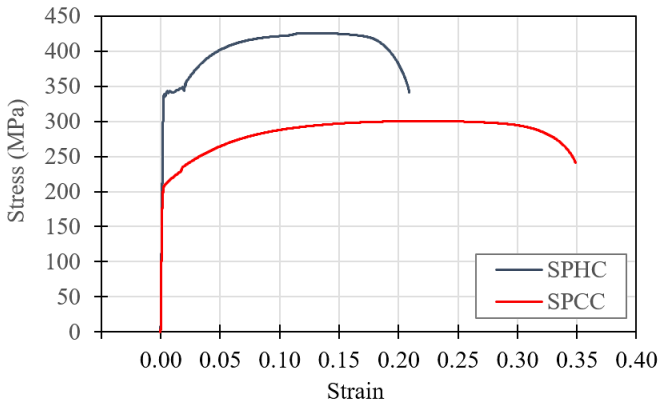

Figure 11. Stress-strain relation curves for SPCC and SPHC

Table 2. SPCC and SPHC mechanical properties

Mechanical Properties	SPCC	SPHC
f_y (MPa)	214.33	341.17
$f_{y(0.2\%)}$ (MPa)	209.46	337.41
f_u (MPa)	300.33	425.72
Elongation (%)	35.5	21.2

3.2. Hysteretic Curve, Shear Strength, and Stiffness of CHSD

Figure 12 presents the hysteretic and backbone curves of the CHSD specimens obtained from cyclic testing, while the summary of the test results is provided in Table 3. The figure also includes the theoretical shear yield strength, calculated using Equation 4, as well as the shear strength and displacement of the CHSD at yielding and ultimate conditions. For comparison, the theoretical shear yield strengths were 65.65 kN for CHSD-NF, 80.24 kN for CHSD-F-0/CHSD-F-G-0, and 79.29 kN for CHSD-F-30/CHSD-F-G-30, as indicated by the dashed lines in Figure 12. Relative differences of 21.41%, 22.85%, and 27.54% were observed compared to the experimental results. These discrepancies arise because the theoretical values are determined at the initial yield stress, whereas the experimental yield strengths were defined using the equivalent elastoplastic yield method (see Figure 10). As shown in Figures 12-a to 12-c, the shear resistance of the CHSD specimens without gaps was mobilised from the beginning of the test until yielding, followed by plastic deformation. In contrast, for the CHSD specimens with gaps (Figures 12-d and 12-e), the hysteretic curves remained nearly flat along the displacement axis. In this case, the loading frame moves freely within the gaps without inducing shear resistance in the specimen. Figure 12-f compares the backbone curves of CHSD specimens with and without gaps. The results show that all specimens without gaps yielded and experienced plastic deformation, whereas shear resistance was not engaged in the specimens with gaps. This indicates that the presence of gaps delays the occurrence of shear resistance and deformation.

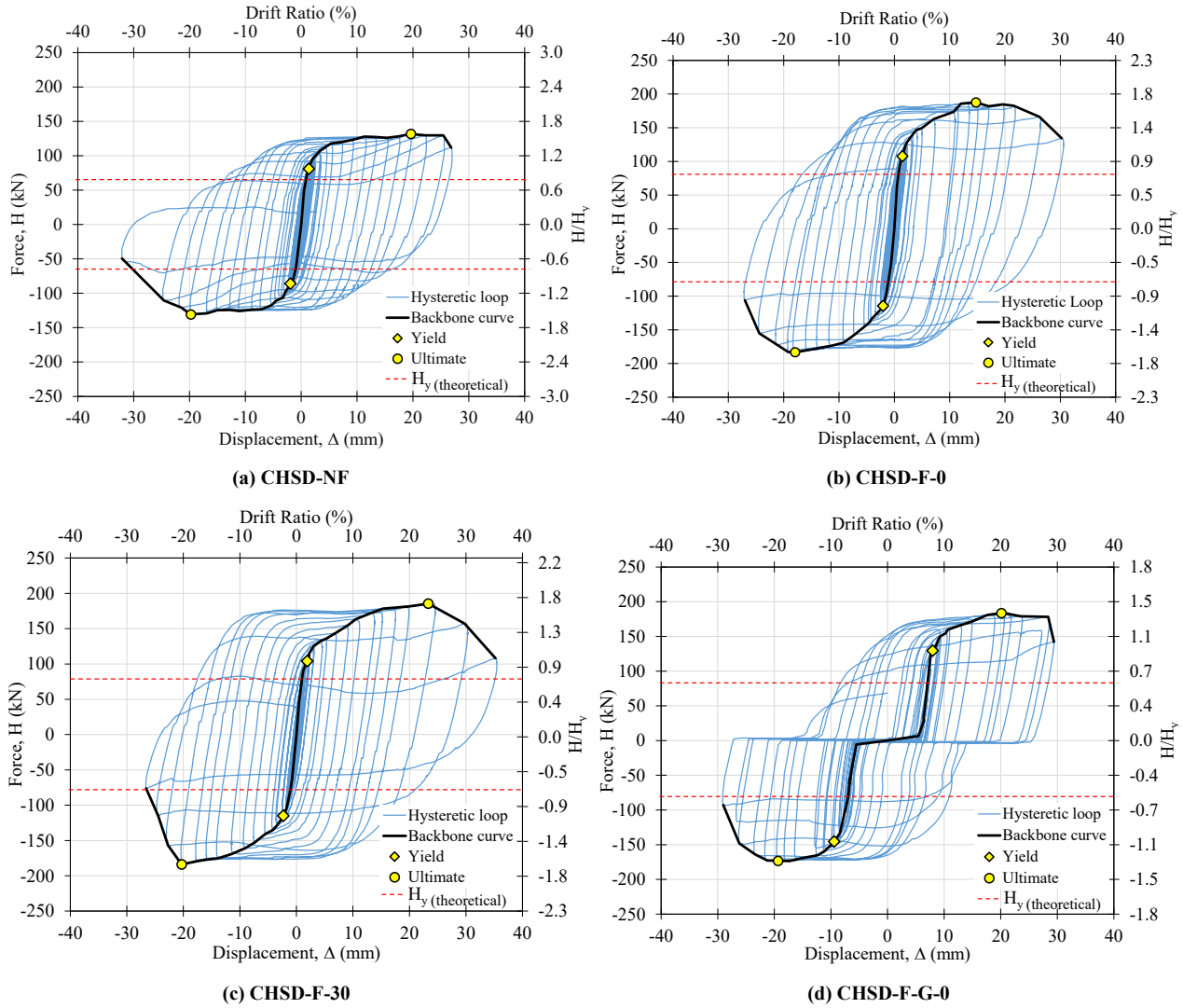

(a) CHSD-NF

(b) CHSD-F-0

(c) CHSD-F-30

(d) CHSD-F-G-0

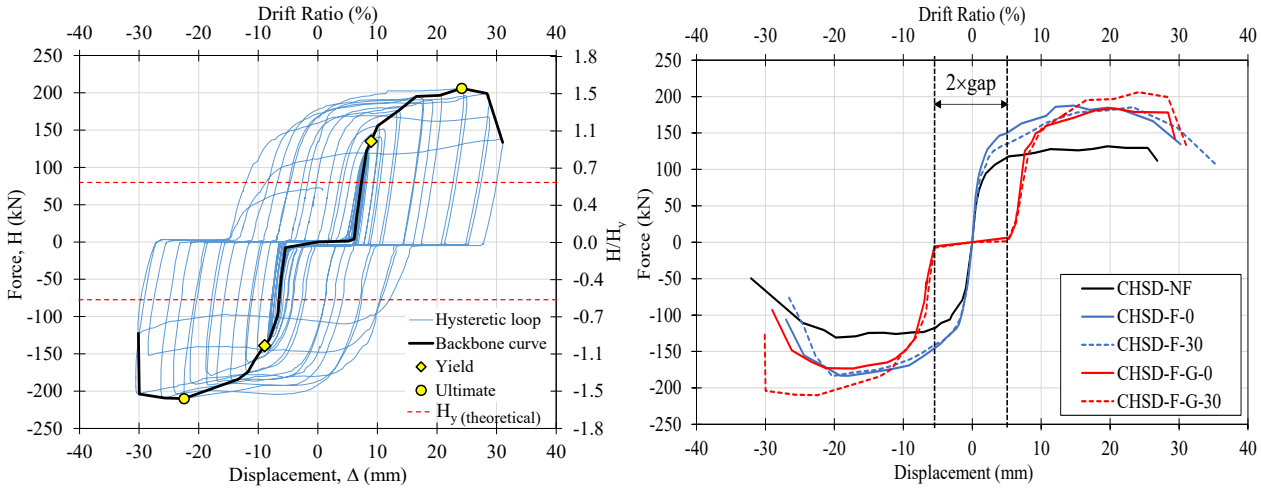

(e) CHSD-F-G-30 **(f) Comparison of backbone curves**

Figure 12. Hysteretic curve and backbone curve

Table 3. CHSD cyclic test results

Specimen name	H_y	Δ_y	Δ_g	$\Delta_y-\Delta_g$	H_u	Δ_u	$\Delta_u-\Delta_g$	Stiffness	*Drift ratio max.*
	(kN)	(mm)	(mm)	(mm)	(kN)	(mm)	(mm)	(kN/mm)	(%)
Positive direction									
CHSD-NF	80.95	1.35	-	-	131.69	19.61	-	60.09	19.61
CHSD-F-0	107.76	1.43	-	-	187.64	14.73	-	75.31	14.73
CHSD-F-30	104.01	1.91	-	-	185.49	23.32	-	54.60	23.32
CHSD-F-G-0	129.57	7.97	5.47	2.50	183.70	20.13	14.66	51.78	14.66
CHSD-F-G-30	135.05	8.94	6.11	2.83	205.99	24.13	18.02	47.68	18.02
Negative direction									
CHSD-NF	-86.14	-1.94	-	-	-130.81	-19.79	-	44.49	19.79
CHSD-F-0	-114.50	-2.05	-	-	-183.31	-17.95	-	55.80	17.95
CHSD-F-30	-114.86	-2.32	-	-	-183.89	-20.29	-	49.55	20.29
CHSD-F-G-0	-145.22	-9.42	5.50	-3.92	-173.13	-19.34	-13.84	37.02	13.85
CHSD-F-G-30	-139.10	-8.92	5.44	-3.48	-210.09	-22.46	-17.03	39.90	17.03

Note: Δ_y = Yield displacement; Δ_g = Measured gap length; H_y = Yield strength; Δ_u = Ultimate displacement; H_u = Ultimate strength

3.2.1. The Influence of Additional Fins

From the comparison of the backbone curves of the specimen without gaps (Figure 12-f), an increase in shear strength was observed in CHSD-F compared to CHSD-NF. The yield strength of the non-finned specimen initially ranged from 80.95 to 86.14 kN. After adding fins, the yield strength increased by 32.93–33.13% for the CHSD-F-0 and 28.49–33.35% for the CHSD-F-30. Furthermore, CHSD-F achieved the highest yield strength at 114.86 kN. The addition of fins also enhanced the ultimate shear strength of the CHSD specimen, with an increase of 40.13–42.48% for the CHSD-F-0 and 40.58–40.85% for the CHSD-F-30. The highest ultimate shear strength was recorded for the CHSD-F-0 specimen, reaching 145.22 kN. Based on these results, adding fins effectively improved shear strength due to the increase in the effective cross-sectional area resisting shear force.

The yield displacement of the CHSD-NF specimen was the lowest among all specimens, ranging from 1.35 to 1.94 mm (Table 3). This suggests that under the same loading conditions, CHSD-NF yielded earlier than others. After adding fins, the yield displacement increased to 1.43–2.05 mm and 1.91–2.32 mm for the CHSD-F-0 and CHSD-F-30, respectively. This corresponds to 5.99–6.24% increases and 19.73–41.43% for the two specimens. Therefore, adding fins to the CHSD specimen increased the yield displacement. The effect of fins on ultimate displacement depended on the loading direction. Compared to CHSD-F-30, adding fins with a loading direction of 30° increases the ultimate displacement by 18.89%. However, adding fins with a loading direction of 0° caused a significant decrease by approximately 24.93%. This behavior demonstrated that the presence of fins significantly influenced stress distribution within the circular components. Under a 0° loading direction, lateral deformation was predominantly resisted by the fin plates, leading to elevated stress concentrations and crack initiation, thereby reducing the ductility of the CHSD. In contrast, under a 30° loading direction, the circular components primarily accommodated lateral deformation, while the fins delayed local buckling, ultimately enhancing the overall deformation capacity of the CHSD.

Adding fins under a 0° loading direction increased specimen stiffness. As shown in Table 3, the stiffness of CHSD-NF ranged from 44.49 to 60.09 kN/mm. After adding fins at a 0° direction (CHSD-F-0), the stiffness increased to 49.55–75.31 kN/mm, corresponding to an increase of 11.37–25.32%. However, this stiffness improvement was only observed under a 0° loading direction, while the stiffness decreased for CHSD-F-30. This variation was influenced by the orientation of the fins relative to the loading direction. For the specimen with a 0° loading direction, fins positioned at 0° and 60° to the x-axis increased the section moment of inertia, thereby enhancing stiffness. In contrast, for the 30° loading direction, only fins positioned at 30° to the x-axis contributed to stiffness, while fins at 90° provided no significant effect.

3.2.2. The Influence of Additional Gaps

The stiffness of the CHSD-F-G specimen ranged from 37.02 to 51.78 kN/mm. Compared to CHSD-F, the introduction of gaps reduced stiffness by approximately 12.67–33.65% due to the contact between the top base plate and the stopper plate. The yield strength of the CHSD-F-G ranged from 129.57 to 145.22 kN, which was 20.24–29.84% higher than that of CHSD-F. This higher yield strength is attributed to the use of the equivalent elastoplastic yield method (see Figure 10) [39], while the introduction of gaps reduced stiffness. The lower stiffness resulted in higher yield strength and increased the displacement of CHSD-F-G by 48.67–91.14% compared to CHSD-NF. Furthermore, the ultimate strength of the CHSD-F-G increased by 11.05–14.25% under a 30° loading direction. In contrast, at a 0° loading direction, the ultimate strength showed a slight decrease of 2.10–5.55%.

The loading direction did not significantly affect the yield strength of the CHSD specimens. As shown in Table 3, the yield strength of CHSD-F and CHSD-F-G specimens under a 0° loading direction was comparable to that under 30°. Similarly, the loading direction had little influence on the ultimate strength of CHSD specimens with fins. However, for CHSD specimens with fins and gaps, loading at 30° resulted in a higher ultimate strength than 0°, with an increase ranging from 12.4% to 21.35%. The reason for this increase at the 30° direction has not yet been identified and requires further investigation. In addition, the loading direction contributed to the larger yield and ultimate displacements at 30° compared to 0°.

3.3. Energy Dissipation Behavior

A comparison of energy dissipation curves obtained from cyclic testing is presented in Figure 13 and Table 4. All test specimens exhibited elastic behavior during the initial loading phase, without a significant loss in energy. The energy dissipation remained relatively constant at the beginning of the loading cycles. As the cycles progressed, the energy dissipation increased until reaching its ultimate value. The energy dissipation capacity of the CHSD-NF specimen was 6.93 kN·m, the lowest among all the specimens. After the addition of fins, the energy dissipation capacity increased to 11.88 kN·m (CHSD-F-0) and 12.57 kN·m (CHSD-F-30), representing a 71.53-81.53% improvement. Therefore, the addition of fins significantly enhanced the energy dissipation capacity of the CHSD, consistent with the findings of previous studies [25, 26]. Further experimental results demonstrate the effect of gaps on energy dissipation capacity, with the impact depending on the loading direction. The CHSD-F-G-30 specimen achieved the highest energy dissipation capacity of 14.01 kN·m. Compared to CHSD-F, the energy dissipation capacity of CHSD-F-G-30 increased by 11.41%, whereas CHSD-F-G-0 exhibited a decrease of 8.9%, with a value of 10.82 kN·m.

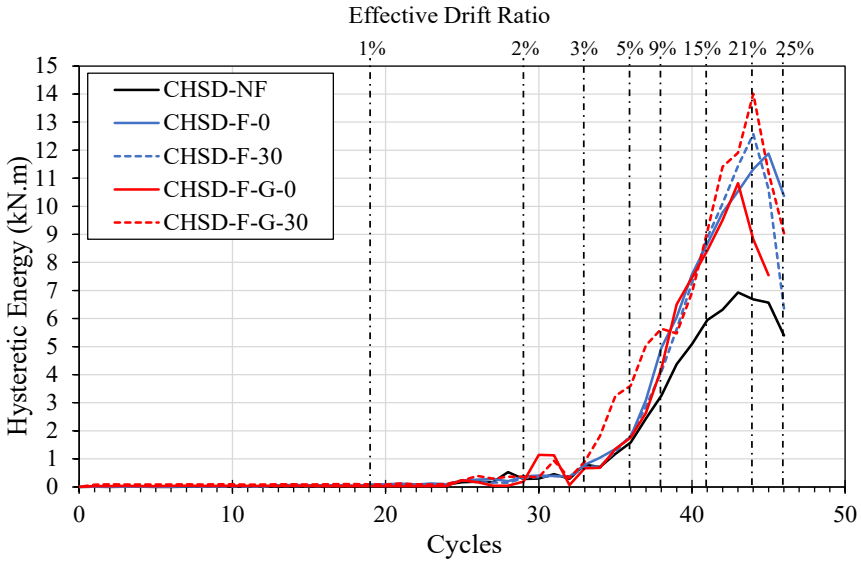

Figure 13. Comparison of energy dissipation curves

Table 4. The maximum hysteretic energy (E_{max}) and equivalent viscous damping ratio (ξ_{max})

Specimen name	E_{max} (kN.m)	ξ_{max} (%)
CHSD-NF	6.93	49.66
CHSD-F-0	11.88	51.37
CHSD-F-30	12.57	54.52
CHSD-F-G-0	10.82	38.01
CHSD-F-G-30	14.01	38.79

3.4. Equivalent Viscous Damping Ratio

As shown in Figure 14, CHSD-F exhibited a slightly higher equivalent viscous damping ratio (ξ_{max}) than CHSD-NF. The equivalent viscous damping ratio of CHSD-F ranged from 51.37% to 54.52%, whereas that of CHSD-NF was 49.66%. This suggests that the addition of fins increased the equivalent viscous damping ratio of the CHSD, although not significantly, with improvements ranging from 3.4% to 9.78%. Similar results were reported by Emilidardi et al. [26], where the hysteretic damping capacity achieved ranged from 52% to 55%.

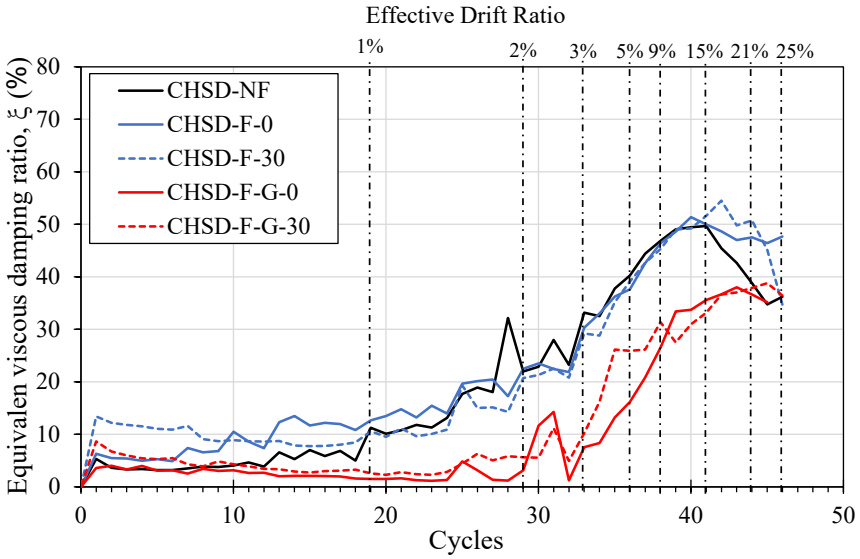

Figure 14. Comparison of equivalent viscous damping ratio

CHSD-F-G exhibited a lower equivalent viscous damping ratio than the specimen without gaps. The damping ratios of CHSD-F-G-0 and CHSD-F-G-30 were 38.01% and 38.79%, respectively, representing a reduction of 26.02% to 28.85% compared to CHSD-F. This indicates that introducing gaps reduces the equivalent viscous damping ratio of CHSD, as the gap prevents the damper from engaging at the onset of cyclic loading and allows activation only after the gap is exceeded. Consequently, the energy absorbed by CHSD specimens with gaps is reduced, as is the hysteresis loop area, leading to a lower damping ratio than specimens without gaps. Nevertheless, the equivalent viscous damping ratio of CHSD with gaps remains higher than that of other dampers, such as LRB900 (lead-core rubber bearings, 900 mm in diameter), with equivalent damping ratios of 19–24%, 17–39%, and 23–35% at shear strains of 50%, 100%, and 250%, respectively [41], and HDRB (high-damping rubber bearings), with effective damping ratios of 22.3–24.7% under 5 MPa vertical compression and 27.7–29.5% under 12 MPa [42]. Moreover, the primary function of the gap in preventing damper fatigue damage under small cyclic loads is effectively achieved, as the gap mechanism delays the initial engagement of the damper in resisting shear force, thereby reducing premature degradation, mitigating the risk of fatigue failure, and ultimately extending the device's service life. Therefore, the proposed CHSD configuration with gaps remains suitable for application as an energy dissipation device in bridge structures, particularly in enhancing long-term seismic resilience.

Another conclusion to be drawn from Figure 14 is that variations in loading direction do not significantly affect the equivalent viscous damping ratio of the specimens. This finding suggests that the CHSD can provide reliable damping capacity regardless of the orientation of lateral seismic forces, proving advantageous for practical bridge applications where earthquake loading is inherently multidirectional.

3.5. Deformation Behavior and Failure Modes

Based on visual observations, the CHSD-NF specimen experienced out-of-plane buckling in the middle section of the tube when the drift ratio reached 9%. As the drift ratio increased to 13%, the out-of-plane buckling became more pronounced, forming a horizontal crack on the lower side of the tube. Subsequently, a crack developed on the upper side of the tube when the drift ratio reached 15.1%. Finally, the ultimate shear strength was attained at a drift ratio of 19.6%. The failure mode of the CHSD-NF specimen is shown in Figure 15.

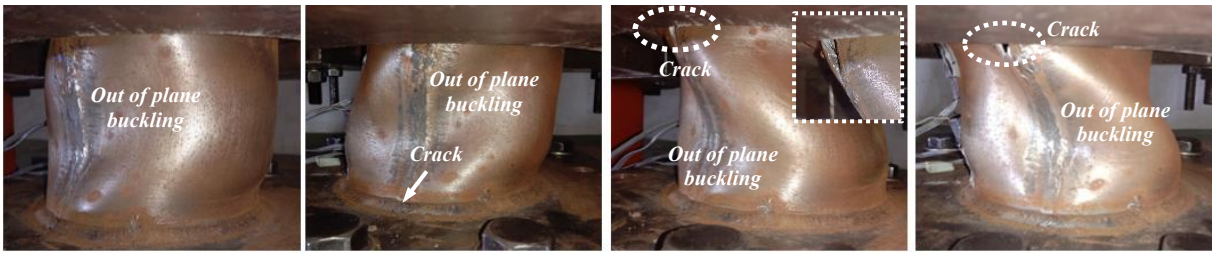

(a) *Drift ratio* 9% (b) *Drift ratio* 13% (c) *Drift ratio* 15.1% (d) *Drift ratio* 19.2%

Figure 15. The failure mode of the CHSD-NF specimen

The CHSD-F-0 specimen experienced out-of-plane buckling when the drift ratio reached 11%. The ultimate shear strength was attained at a drift ratio of 14.72%. Cracking initially appeared at the lower part of the fins when the drift ratio reached 21.3%, while the tube only exhibited out-of-plane buckling. For comparison, in the CHSD-NF specimen, cracking developed earlier, at a drift ratio of 13%. This indicates that adding fin plates can delay buckling and cracking. As the drift ratio increased to 23.4%, the cracks widened, leading to failure at the junction between the tube and the fin plates. The failure mode of the CHSD-F-0 specimen is shown in Figure 16.

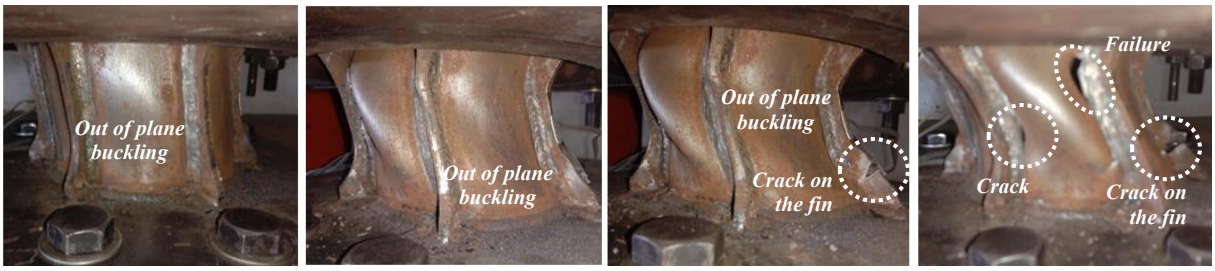

(a) *Drift ratio* 11% (b) *Drift ratio* 14.7% (c) *Drift ratio* 21.3% (d) *Drift ratio* 23.4%

Figure 16. The failure mode of the CHSD-F-0 specimen

At a drift ratio of 13%, the CHSD-F-30 specimen experienced out-of-plane buckling. As the drift ratio increased to 17%, the out-of-plane buckling became more pronounced, while no cracks were observed in either the tube or fins. A vertical crack first appeared at the connection between the tube and the fins when the drift ratio reached 21.3%, after which the ultimate shear strength was attained at 23.3%. At this stage, damage occurred in the tube without visible cracking. The failure mode of the CHSD-F-30 specimen is shown in Figure 17.

(a) *Drift ratio* 13% (b) *Drift ratio* 17% (c) *Drift ratio* 21.3% (d) *Drift ratio* 23.4%

Figure 17. The failure mode of the CHSD-F-30 specimen

In the CHSD-F-G-0 specimen, the tube experienced buckling and a crack formed at the lower end of the fin plate when the drift ratio reached 14.7%. At this stage, the specimen also reached its ultimate strength. As the drift ratio increased to 17.1%, damage appeared at the tube connection, and the crack in the fin plate propagated further. Subsequently, as the drift ratio reached 19.2%, damage to the tube and the fin plate became more severe. The failure mode of the CHSD-F-G-0 specimen is shown in Figure 18.

(a) *Drift ratio* 14.7% (b) *Drift ratio* 17.1% (c) *Drift ratio* 19.2%

Figure 18. The failure mode of the CHSD-F-G-0 specimen

The CHSD-F-G-30 specimen experienced out-of-plane buckling when the drift ratio reached 14.4%, and achieved its ultimate shear strength at 18%. At this stage, an initial crack appeared at the bottom of the tube. As the drift ratio increased to 18.7%, additional cracking developed on the fin plate, and the crack at the bottom of the tube further propagated. The failure mode of the CHSD-F-G-30 specimen is shown in Figure 19.

(a) *Drift ratio* 14.4% (b) *Drift ratio* 18% (c) *Drift ratio* 18.7%

Figure 19. The failure mode of the CHSD-F-G-30 specimen

4. Finite Element Analysis with Monotonic Loading

Finite element analysis (FEA) was conducted to verify the numerical model developed for all CHSD specimens. The modelling was carried out in Abaqus with a monotonic load applied. This loading condition was adopted to simplify the model, considering that the SPCC and SPHC material tests were based on monotonic tensile testing without corresponding cyclic parameters. The numerical results were then compared with the experimental results to verify the proposed model.

4.1. Numerical Modelling

The numerical model of the CHSD specimen is shown in Figure 20. The circular hollow component was modelled using continuum shell elements, specifically the SC8R element. This element type was adopted because the tube thickness is much smaller than its other dimensions, and the stress perpendicular to the tube plane direction was neglected. A single-element layer was applied through the plate thickness to account for the relatively small wall thickness and to enhance computational efficiency. Fin and baseplate components were modelled using solid elements, specifically the C3D8R element. A mesh size of 5 mm was used for the tube and fin components. The contact between the tube, fin, and baseplate components was modelled using a surface-to-surface tie constraint to idealize a fixed connection. Therefore, the welding effect was neglected in the numerical model. To accommodate the presence of gaps, the contact surfaces between the upper baseplate, stopper plate, and locking plate were modelled using surface-to-surface contact. The behavior in the normal direction was modelled with "hard contact" to prevent penetration. In contrast, the behavior in the tangential direction was defined as "frictionless", friction between surfaces was not considered, thereby allowing baseplate movement along the gaps.

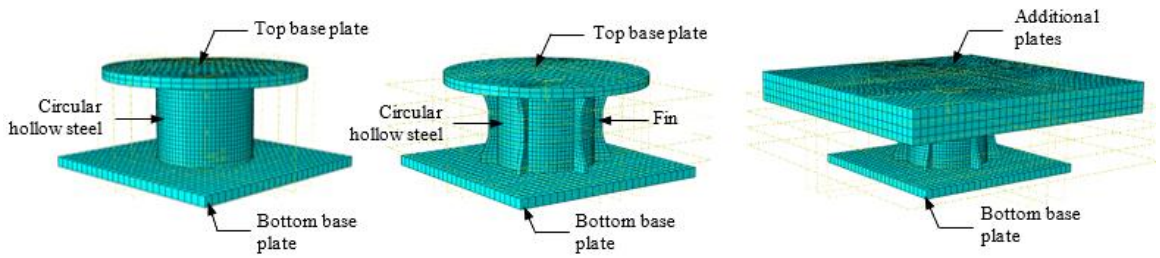

(a) (b) (c)

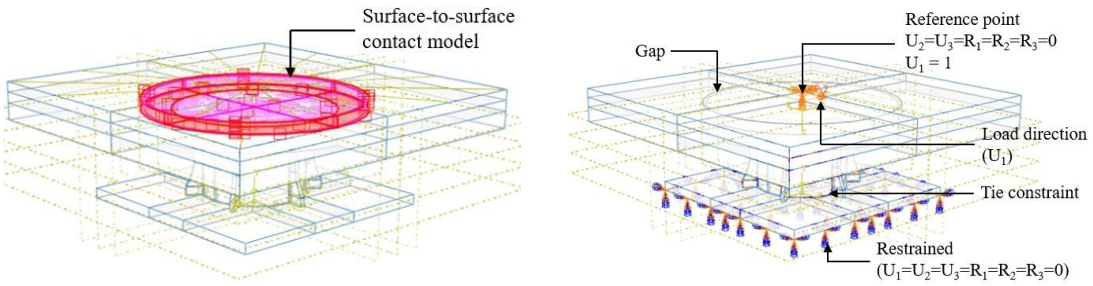

(d) (e)

Figure 20. Numerical model of CHSD in Abaqus: (a) model without fins, (b) model with fins, (c) model with fins and additional plate installation on the top base plate, (d) surface-to-surface contact model, and (e) boundary condition and load direction

The monotonic load was applied at the centroid of the upper additional plate along the U_1 axis under displacement control, with the target displacement set equal to the ultimate displacement obtained from the cyclic tests. The additional plate was constrained to translate only in the U_1 direction, while all other translational and rotational degrees of freedom were restrained. The CHSD base plate was fully fixed in all directions.

4.2. Steel Material Modelling

As defined in the numerical modelling, the material properties of SPCC and SPHC steel consist of elastic and plastic parameters. For the plastic parameters, the stress-strain curve obtained from tensile testing of the steel plate (Figure 11) was converted into a true stress-strain curve (Figure 21). This conversion was essential to accommodate the shape change and reduction in the cross-sectional area after necking. The baseplate component and additional plates were modelled using S355 steel material. The elastic and plastic properties of S355 were adopted from the true stress–strain parameters reported by Narendra et al. [43] (Table 5). Strain-hardening characteristics were particularly important for modelling the CHSD specimens in the plastic range. In this study, strain hardening was modelled using a combined isotropic/kinematic hardening model, which was considered best for simulating SPD behavior [44].

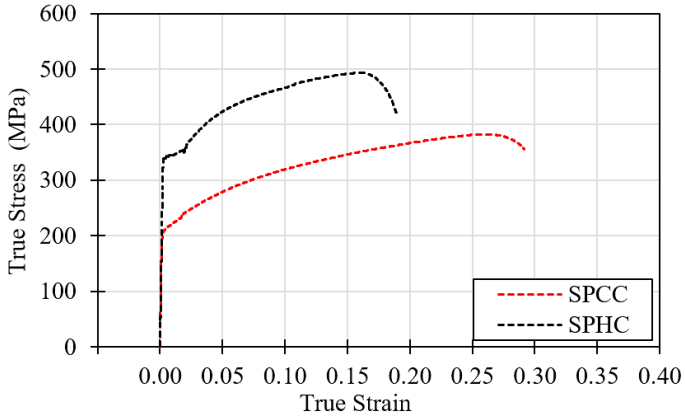

Figure 21. True stress-strain curve of SPCC and SPHC

Table 5. Material properties of S355 [43]

Material	E (MPa)	$\sigma\|_0$	C_1 (MPa)	γ_1	C_2 (MPa)	γ_2	C_3 (MPa)	γ_3	υ
S355	185000	386	5327	75	1725	16	1120	10	0.3

Note: E = Elastic modulus; $\sigma|_0$ = Yield stress at zero plastic strain; C_1, C_2, C_3 = Kinematic hardening modulus; γ_1, γ_2, γ_3 = The rate of kinematic hardening modulus; ν = Poisson's ratio.

4.3. Validation of Numerical Results with Experimental Results

The backbone curve obtained from the numerical analysis for all CHSD specimens without gaps showed good agreement with the experimental results (Figures 22-a to 22-c). However, a noticeable discrepancy was observed in the backbone curve of the CHSD specimens with gaps, particularly for the CHSD-F-G-30 (Figure 22-e). The stiffness derived from the numerical analysis was higher than that measured in the experiments. This difference can be attributed to the compliance of the loading frame, which caused part of the applied displacement to be absorbed by the testing apparatus rather than the specimen. In addition, the anchorage stiffness of the base plate to the rigid floor may have contributed to this discrepancy, even though the anchor bolts were tightened with a torque wrench.

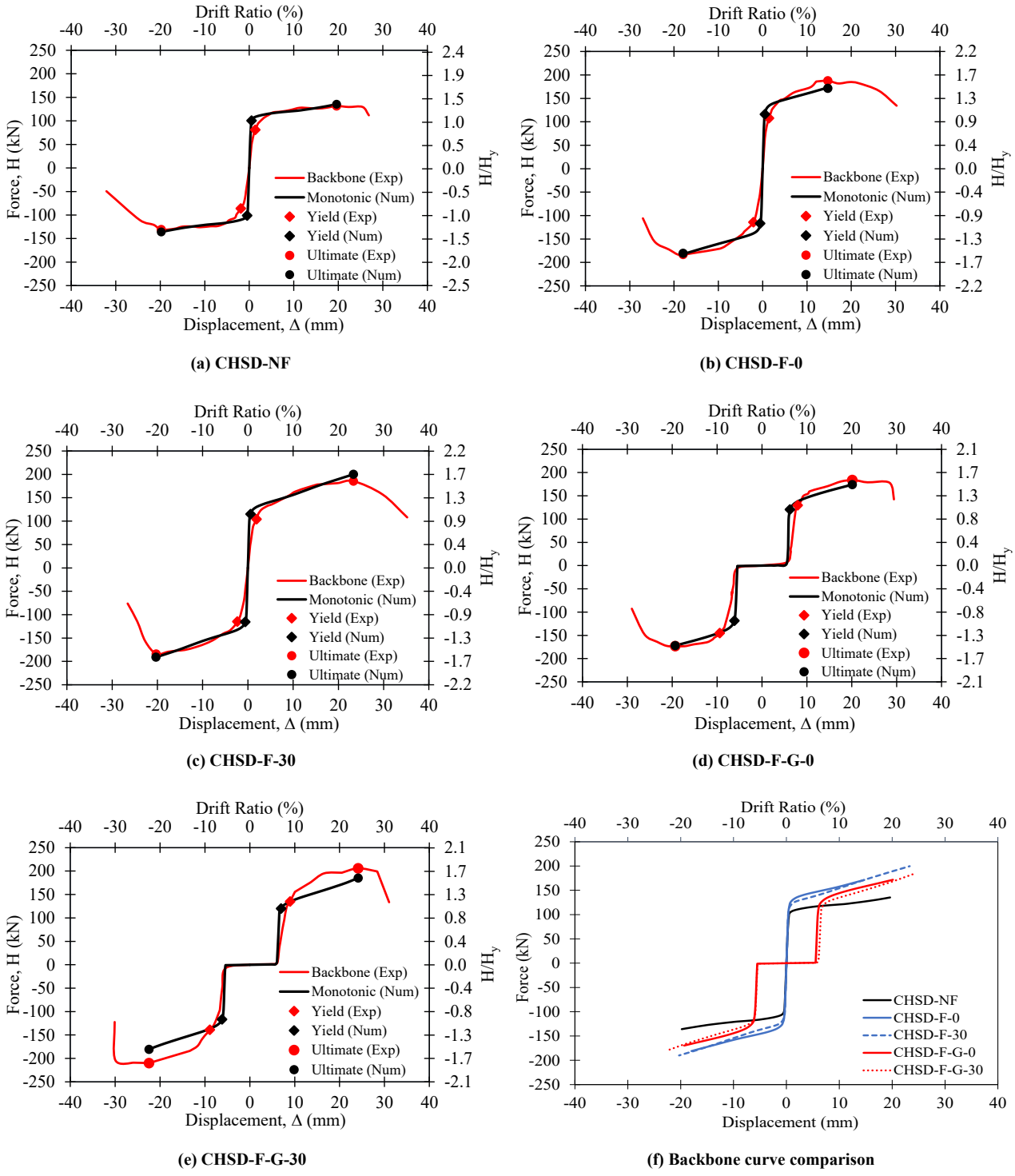

Figure 22. Backbone curve from the numerical analysis results

A summary of the numerical analysis results and their comparison with the experimental findings is presented in Table 6. For CHSD specimens with gaps, the displacements listed in the table were adjusted by subtracting the gap length. The numerical analysis showed that the yield displacement of all CHSD specimens ranged from 0.49 mm to 0.87 mm, with the highest value observed for CHSD-F-G-30. The shear yield strength of the specimens ranged from 100.59 kN to 121.02 kN, while the ultimate strength varied between 130.81 kN and 210.09 kN. The addition of fins increased both yield strength and ultimate strength by 13.61%–15.71% and 26.40%–47.37%, respectively. In contrast, the presence of gaps and variations in loading direction did not significantly influence yield or ultimate strength.

Table 6. Comparison of experimental test results with numerical analysis

Specimen name	Experiment		Numeric		Relative differences		Experiment		Numeric		Relative differences
	Δ_y (mm)	H_y (kN)	Δ_y (mm)	H_y (kN)	Δ_y (%)	H_y (%)	Δ_u (mm)	H_u (kN)	Δ_u (mm)	H_u (kN)	H_u (%)
Positive direction											
CHSD-NF	1.35	80.95	0.49	100.59	63.62	24.27	19.61	131.69	19.61	135.41	2.82
CHSD-F-0	1.43	107.76	0.54	115.85	62.26	7.50	14.73	187.64	14.73	171.17	8.78
CHSD-F-30	1.91	104.01	0.60	115.20	68.50	10.76	23.32	185.49	23.32	199.54	7.58
CHSD-F-G-0	2.50	129.58	0.76	121.02	69.63	6.60	14.66	183.70	14.61	171.84	6.46
CHSD-F-G-30	2.83	135.05	0.87	118.77	69.28	12.05	18.02	205.99	18.06	183.88	10.74
Negative direction											
CHSD-NF	-1.94	-86.14	-0.50	-101.09	74.17	17.36	-19.79	-130.81	-19.79	-135.97	3.95
CHSD-F-0	-2.05	-114.50	-0.56	-116.97	72.71	2.16	-17.95	-183.31	-17.95	-180.84	1.35
CHSD-F-30	-2.32	-114.86	-0.58	-114.85	74.98	0.01	-20.29	-183.89	-20.30	-189.92	3.28
CHSD-F-G-0	-3.92	-145.22	-0.75	-120.66	80.88	16.91	-13.84	-173.13	-13.82	-169.78	1.94
CHSD-F-G-30	-3.49	-139.10	-0.68	-114.81	80.49	17.46	-17.03	-210.09	-16.98	-179.55	14.54

Note: Δ_y = Yield displacement; H_y = Yield strength; Δ_u = Ultimate displacement; H_u = Ultimate strength

Figure 23 presents the deformation shape of the specimen from cyclic testing, as well as shear stress (S12) and maximum stress contours obtained from numerical analysis for the yielding condition. Meanwhile, Figure 24 illustrates the deformation at the ultimate condition. In the yielding condition, shear stress (S12) distribution is observed across most of the circular hollow tube surfaces of all specimens, while no significant shear stress is yet observed in the fin area. The maximum stress is concentrated on the fin plates adjacent to the loading location, with the highest stress occurring on the fin plate at the 0° loading direction. The distribution of maximum stress extends from the tip of the fin plate to the curved transition area.

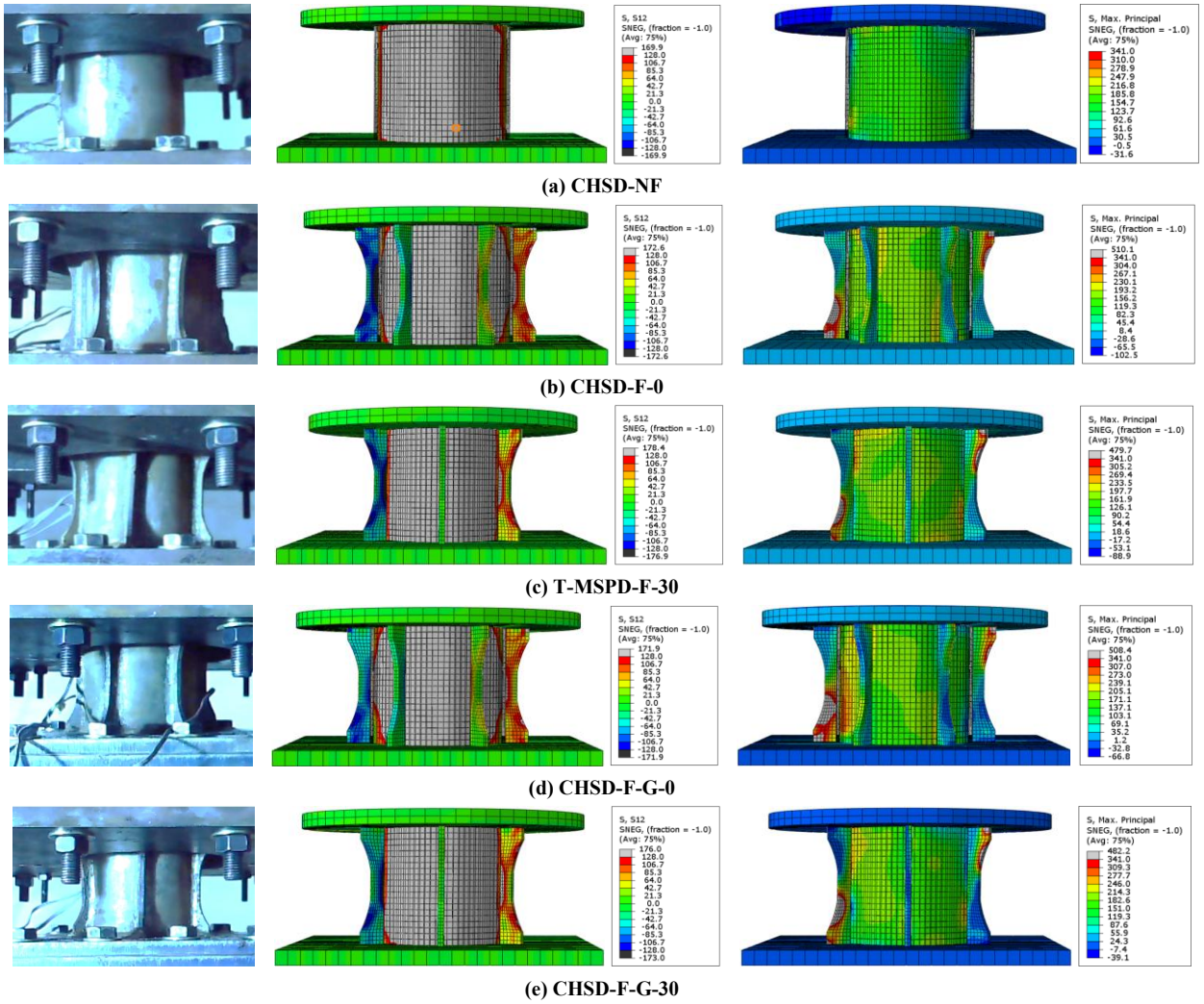

(a) CHSD-NF

(b) CHSD-F-0

(c) T-MSPD-F-30

(d) CHSD-F-G-0

(e) CHSD-F-G-30

Figure 23. Deformation shape of the test specimens, shear stress contours, and maximum stress contours from the numerical analysis at the yield condition

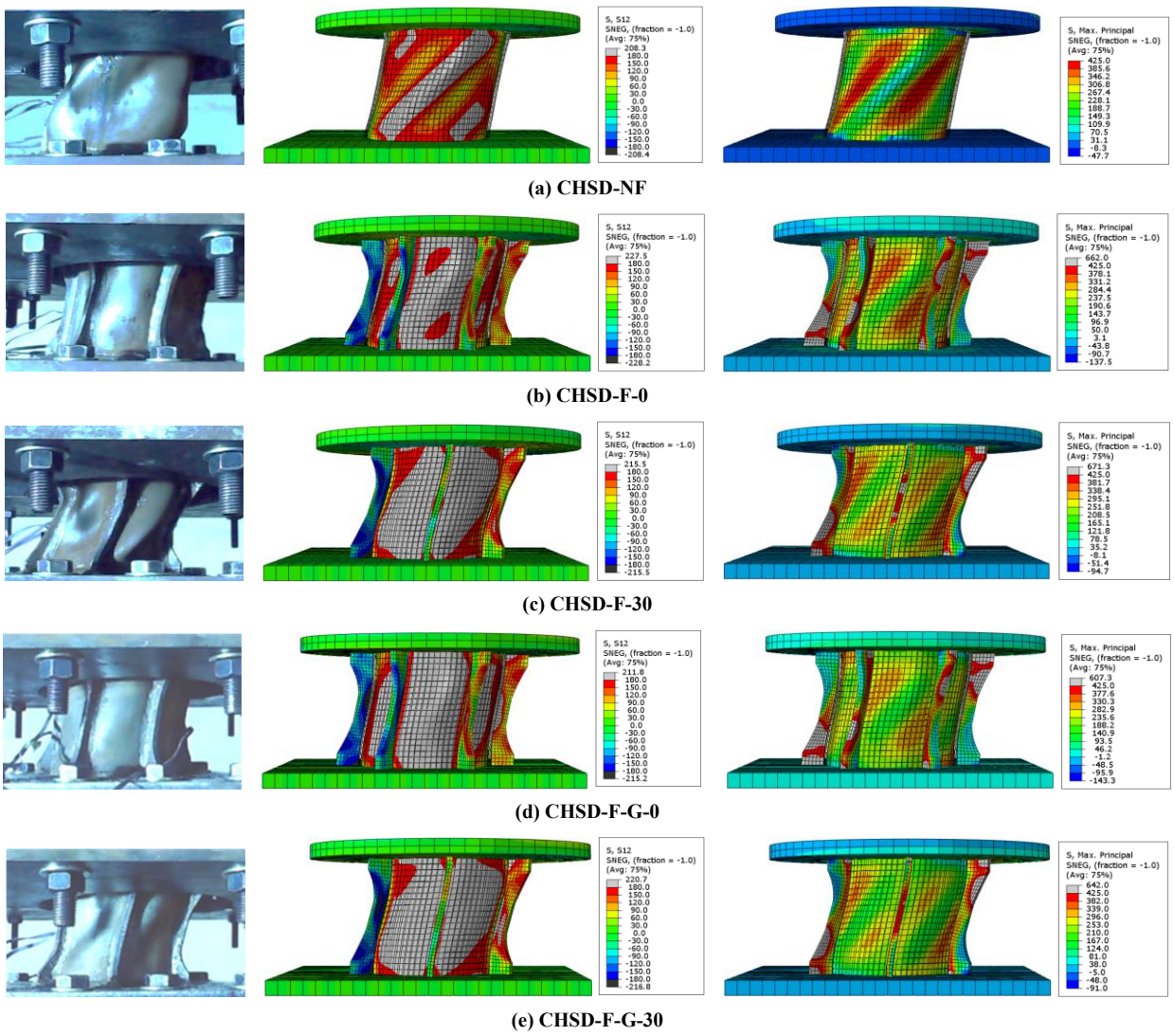

Figure 24. Deformation shape of the test specimens, shear stress contours, and maximum stress contours from the numerical analysis at the ultimate condition

In the ultimate condition, shear stress in the hollow circular component increased significantly, leading to severe out-of-plane buckling. The shear stress distribution also expanded into the fin area, resulting in buckling of the fin plates. For the CHSD specimen loaded at 0°, the maximum stress concentration occurred at the curved transition section extending to the tip of the fins. In contrast, for the specimen loaded at 30°, the stress concentration was located at the tip of the circular hollow component or at its junction with the base plate. The stress concentration exceeds the material's ultimate stress. These findings are validated by experimental results, showing that the CHSD specimen with a 0° loading direction experienced a fracture in the curved transition section of fins. Additionally, the deformation predicted by the numerical analysis is approximately identical to the deformation obtained from the experimental results.

5. Conclusions

This study investigated the potential of CHSD with the incorporation of fins and gaps. Both experimental testing and numerical analysis were conducted to evaluate the mechanical behavior and seismic performance of CHSD, achieving the following results:

- The addition of fins to the CHSD enhanced shear strength, stiffness, and energy dissipation capacity. The maximum yield strength was achieved at a 0° loading direction, whereas the highest energy dissipation capacity occurred at 30°. Adding fins also slightly improved the equivalent viscous damping ratio, while variations in loading direction had no significant effect on this parameter.
- Yield displacement was also increased, with fins under a 30° loading direction producing higher values. Meanwhile, the influence of fins on ultimate displacement depended on the loading direction. The addition of fins at 0° reduced the ultimate displacement, while at 30° caused a significant increase.

- The presence of gaps in the CHSD specimen reduced stiffness and the equivalent viscous damping ratio. Furthermore, the effect of gaps on energy dissipation capacity depended on the loading direction, with an increase observed under a 30° loading direction.
- Although CHSD with gaps exhibited a lower equivalent viscous damping ratio compared to other specimens, the introduction of gaps effectively delayed shear resistance and deformation. Consequently, the CHSD with gaps has the potential to mitigate fatigue-induced damage.
- The proposed numerical model of the CHSD shows satisfactory accuracy, with good agreement between the backbone curve, deformation shape, and stress contours from numerical and experimental results. However, the shear yield strength from the backbone curve ranges from 21.41% to 27.54% higher than the theoretical initial value.
- The proposed CHSD with fins and gaps shows practical applicability for bridge structures, as it can delay damper activation under small cyclic loads. This capability reduces the risk of fatigue-related damage and extends service life, while ensuring adequate energy dissipation during major seismic events.

6. Declarations

6.1. Author Contributions

Conceptualization, I.S., A.A., and T.S.M.A.; methodology, A.F.S., I.S., and T.S.M.A.; software, A.F.S. and T.S.M.A.; validation, I.S., A.A., and A.F.S.; formal analysis, T.S.M.A.; investigation, T.S.M.A., A.A., and A.F.S.; resources, A.F.S.; data curation, A.A.; writing—original draft preparation, T.S.M.A. and A.F.S.; writing—review and editing, T.S.M.A., I.M.S., A.A., and A.F.S.; visualization, A.F.S.; supervision, I.M.S. and A.A.; project administration, A.A. and T.S.M.A.; funding acquisition, A.A. All authors have read and agreed to the published version of the manuscript.

6.2. Data Availability Statement

The data presented in this study are available in the article.

6.3. Funding and Acknowledgments

The authors are grateful to the Research Directorate of Universitas Gadjah Mada for the support (Grant No. 5286/UN1.P.I/PT.01.03/2024). This type of damper has been officially registered in a patent application with the Ministry of Law of the Republic of Indonesia under patent application number P00202313397.

6.4. Conflicts of Interest

The authors declare no conflict of interest.

7. References

[1] Spencer, B. F., & Nagarajaiah, S. (2003). State of the Art of Structural Control. Journal of Structural Engineering, 129(7), 845–856. doi:10.1061/(asce)0733-9445(2003)129:7(845).

[2] Saaed, T. E., Nikolakopoulos, G., Jonasson, J. E., & Hedlund, H. (2015). A state-of-the-art review of structural control systems. JVC/Journal of Vibration and Control, 21(5), 919–937. doi:10.1177/1077546313478294.

[3] Javanmardi, A., Ghaedi, K., Ibrahim, Z., & Muthu, K. U. (2018). Seismic Pounding Mitigation of an Existing Cable-Stayed Bridge Using Metallic Dampers. IABSE Conference, Kuala Lumpur 2018: Engineering the Developing World, 110, 617–623. doi:10.2749/kualalumpur.2018.0617.

[4] Zhu, B., Wang, T., & Zhang, L. (2018). Quasi-static test of assembled steel shear panel dampers with optimized shapes. Engineering Structures, 172, 346–357. doi:10.1016/j.engstruct.2018.06.004.

[5] Soong, T. T., & Spencer, B. F. (2002). Supplemental energy dissipation: State-of-the-art and state-of-the-practice. Engineering Structures, 24(3), 243–259. doi:10.1016/S0141-0296(01)00092-X.

[6] Symans, M. D., Charney, F. A., Whittaker, A. S., Constantinou, M. C., Kircher, C. A., Johnson, M. W., & McNamara, R. J. (2008). Energy Dissipation Systems for Seismic Applications: Current Practice and Recent Developments. Journal of Structural Engineering, 134(1), 3–21. doi:10.1061/(asce)0733-9445(2008)134:1(3).

[7] Constantinou, M. C., Soong, T. T., & Dargush, G. F. (1998). Passive Energy Dissipation Systems for Structural Design and Retrofit. Multidisciplinary Center for Earthquake Engineering Research (MCEER), New York, United States.

[8] Deng, K., Pan, P., Li, W., & Xue, Y. (2015). Development of a buckling restrained shear panel damper. Journal of Constructional Steel Research, 106, 311–321. doi:10.1016/j.jcsr.2015.01.004.

[9] Tanaka, K., & Sasaki, Y. (2000). Hysteretic performance of shear panel dampers of ultra-low yield-strength steel for seismic response control of buildings. 12th World Conference on Earthquake Engineering, 30 January-4 February, 2000, Auckland, New Zealand.

[10] Zhang, C., Zhang, Z., & Shi, J. (2012). Development of high deformation capacity low yield strength steel shear panel damper. Journal of Constructional Steel Research, 75, 116–130. doi:10.1016/j.jcsr.2012.03.014.

[11] Shi, G., Gao, Y., & Zhao, H. (2021). Research Advances of Low Yield Point Steels in Structures and Codification of Specification in China. 11th International Symposium on Steel Structures, 3-6 November, 2021, Jeju, Korea.

[12] Shi, G., Gao, Y., Wang, X., & Zhang, Y. (2018). Mechanical properties and constitutive models of low yield point steels. Construction and Building Materials, 175, 570–587. doi:10.1016/j.conbuildmat.2018.04.219.

[13] Zhang, C., Zhang, Z., & Zhang, Q. (2012). Static and dynamic cyclic performance of a low-yield-strength steel shear panel damper. Journal of Constructional Steel Research, 79, 195–203. doi:10.1016/j.jcsr.2012.07.030.

[14] Zhang, C., Aoki, T., Zhang, Q., & Wu, M. (2013). Experimental investigation on the low-yield-strength steel shear panel damper under different loading. Journal of Constructional Steel Research, 84, 105–113. doi:10.1016/j.jcsr.2013.01.014.

[15] Zhang, C., Aoki, T., Zhang, Q., & Wu, M. (2015). The performance of low-yield-strength steel shear-panel damper with without buckling. Materials and Structures/Materiaux et Constructions, 48(4), 1233–1242. doi:10.1617/s11527-013-0228-9.

[16] Chen, Z., Ge, H., & Usami, T. (2006). Hysteretic Model of Stiffened Shear Panel Dampers. Journal of Structural Engineering, 132(3), 478–483. doi:10.1061/(asce)0733-9445(2006)132:3(478).

[17] Ge, H. B., Kaneko, K., & Usami, T. (2008). Capacity of stiffened steel shear panels as a structural control damper. 14th World Conference on Earthquake Engineering, 12-17 October, 2008, Beijing, China.

[18] Lin, Y., Yang, S., Guan, D., & Guo, Z. (2020). Modified strip model for indirect buckling restrained shear panel dampers. Journal of Constructional Steel Research, 175, 1–15. doi:10.1016/j.jcsr.2020.106371.

[19] Pan, Y., Gao, H., Zeng, H., & Li, Y. (2024). Study on energy dissipation performance of low-yield-point steel shear panel dampers. Journal of Constructional Steel Research, 213, 108351. doi:10.1016/j.jcsr.2023.108351.

[20] Shang, C., Zhou, Y., Shi, F., Li, J., & Jiang, K. (2024). Investigation on mechanical behavior of shear panel damper under bidirectional loading. Journal of Constructional Steel Research, 216, 108580. doi:10.1016/j.jcsr.2024.108580.

[21] Aoki, T., Liu, Y., Takaku, T., & Fukumoto, Y. (2008). A new type of shear panel dampers for highway bridge bearings. 5th European Conference on Steel and Composite Structures, 3-5 September, 2008, Graz, Austria,.

[22] Fajar, A. S., Darmawan, M. F., Yogatama, B. A., Satyarno, I., & Guntara, M. (2020). Seismic performance investigation of bracing and SPD application in PHC pile as viaduct piers. The 17th World Conference on Earthquake Engineering, 13-18 September, Sendai, Japan.

[23] Ge, H., Chen, X., & Matsui, N. (2011). Seismic demand on shear panel dampers installed in steel-framed bridge pier structures. Journal of Earthquake Engineering, 15(3), 339–361. doi:10.1080/13632469.2010.491892.

[24] Abebe, D. Y., Kim, J. W., Gwak, G., & Choi, J. H. (2019). Low-Cycled Hysteresis Characteristics of Circular Hollow Steel Damper Subjected to Inelastic Behavior. International Journal of Steel Structures, 19(1), 157-167. doi:10.1007/s13296-018-0097-8.

[25] Utomo, J., Moestopo, M., Surahman, A., & Kusumastuti, D. (2017). Applications of vertical steel pipe dampers for seismic response reduction of steel moment frames. MATEC Web of Conferences, 138, 2002. doi:10.1051/matecconf/201713802002.

[26] Emilidardi, A. M., Fajar, A. S., Awaludin, A., Satyarno, I., & Sunarso, M. (2022). Numerical Model of Finned Tubular Shear Panel Damper for Multi-direction Seismic Excitation. Proceedings of the 5th International Conference on Sustainable Civil Engineering Structures and Construction Materials, SCESCM 2020. Lecture Notes in Civil Engineering, 215, Springer, Singapore. doi:10.1007/978-981-16-7924-7_49.

[27] Awaludin, A., Emilidardi, A. M., Setiawan, A. F., & Satyarno, I. (2025). The mechanical behavior of multidirectional finned circular hollow steel damper: Analytical and numerical approach. Steel and Composite Structures, 55(3), 211–224. doi:10.12989/scs.2025.55.3.211.

[28] Zhong, G., He, Z., Chen, H., & Zhou, Y. (2023). Seismic performance of end-reinforced steel pipe dampers: Laboratory test and numerical investigation. Journal of Constructional Steel Research, 208, 107994. doi:10.1016/j.jcsr.2023.107994.

[29] Awaludin, A., Setiawan, A. F., Satyarno, I., Shuanglan, W., & Haroki, Y. (2022). Finite Element Analysis of Bi-directional Shear Panel Damper with Square Hollow Section under Monotonic Loading. Journal of the Civil Engineering Forum, 8(2), 157–168. doi:10.22146/jcef.3842.

[30] Setiawan, A. F., Awaludin, A., Satyarno, I., Md Nor, N., Haroki, Y., Darmawan, M. F., Purnomo, S., & Sumartono, I. H. (2025). Cyclic Behavior of Multidirectional Box-Shaped Shearing Damper: Experimental Study. Journal of the Civil Engineering Forum, 11(2), 203–216. doi:10.22146/jcef.14550.

[31] Bagas, N. U., Satyarno, I., Fajar, A. S., Awaludin, A., & Guntara, M. A. (2022). Finite Element Analysis for Developing Multi-direction Crossing Web Type Shear Panel Damper. Proceedings of the 5th International Conference on Sustainable Civil Engineering Structures and Construction Materials. SCESCM 2020. Lecture Notes in Civil Engineering, 215, Springer, Singapore. doi:10.1007/978-981-16-7924-7_48.

[32] Angga, F. S. (2018). Development of High Seismic Performance Integrated Bridge Pier Connected by Hysterical Damper. PhD Thesis, Kyoto University, Kyoto, Japan. doi:10.14989/doctor.k21085.

[33] Emilidardi, A. M., Awaludin, A., Triwiyono, A., Setiawan, A. F., Satyarno, I., & Santoso, A. K. (2024). Seismic performance enhancement of a PCI-girder bridge pier with shear panel damper plus gap: Numerical simulation. Earthquake and Structures, 27(1), 69–82. doi:10.12989/eas.2024.27.1.069.

[34] Haroki, Y., Awaludin, A., Priyosulistyo, H., Setiawan, A. F., & Satyarno, I. (2023). Seismic Performance Comparison of Simply Supported Hollow Slab on Pile Group Structure with Different Operational Category and Shear Panel Damper Application. Civil Engineering Dimension, 25(1), 10–19. doi:10.9744/ced.25.1.10-19.

[35] Santoso, A. K., Sulistyo, D., Awaludin, A., Setiawan, A. F., Satyarno, I., Purnomo, S., & Harry, I. (2024). Comparative Study of The Seismic Performance Between Simply Supported PSC Box Girder Bridge Equipped with Shear Panel Damper and Lead Rubber Bearing. International Journal of Technology, 15(5), 1321–1330. doi:10.14716/ijtech.v15i5.5750.

[36] SNI 8389:2017. (2017). Metal tensile test method. Badan Standardisasi Nasional (BSN), Jakarta, Indonesia. (In Indonesian).

[37] ANSI/AISC 341-22. (2022). Seismic Provisions for Structural Steel Buildings. American Institute of Steel Construction (AISC), Chicago, United States.

[38] ANSI/AISC 360-16. (2016). Specification for Structural Steel Buildings. American Institute of Steel Construction (AISC), Chicago, United States.

[39] Park, R. (1989). Evaluation of ductility of structures and structural assemblages from laboratory testing. Bulletin of the New Zealand Society for Earthquake Engineering, 22(3), 155–166. doi:10.5459/bnzsee.22.3.155-166.

[40] Zhang, Q., Wei, Z. Y., Gong, J. X., Yu, P., & Zhang, Y. Q. (2018). Equivalent Viscous Damping Ratio Model for Flexure Critical Reinforced Concrete Columns. Advances in Civil Engineering, 2018, 1–15. doi:10.1155/2018/5897620.

[41] Pang, H., Jiang, T., Dai, J., Yang, Y., & Bai, W. (2024). Experimental Study of the Mechanical Properties of Full-Scale Rubber Bearings at 23 °C, 0 °C, and −20 °C. Polymers, 16(7), 903. doi:10.3390/polym16070903.

[42] Li, T., Yang, Y., Xu, J., Dai, K., Ge, Q., Wang, J., Chen, P., Wang, B., & Huang, Z. (2022). Hysteretic behavior of high damping rubber bearings under multiaxial excitation. Soil Dynamics and Earthquake Engineering, 163, 107549. doi:10.1016/j.soildyn.2022.107549.

[43] Narendra, P. V. R., Prasad, K., Krishna, E. H., Kumar, V., & Singh, K. D. (2019). Low-Cycle-Fatigue (LCF) behavior and cyclic plasticity modeling of E250A mild steel. Structures, 20, 594–606. doi:10.1016/j.istruc.2019.06.014.

[44] Abebe, D. Y., Jeong, S. J., Getahune, B. M., Segu, D. Z., & Choi, J. H. (2015). Hysteretic characteristics of shear panel damper made of low yield point steel. Materials Research Innovations, 19(5), 1219. doi:10.1179/1432891714Z.0000000001219.